

Excellent hardening effect in lead-free piezoceramics by embedding local Cu-doped defect dipoles in phase boundary engineering

Received: 18 December 2024

Accepted: 17 March 2025

Published online: 25 March 2025

Check for updates

Xinyue Qiu¹, Chao Wu¹, Daniel Q. Tan²✉, Ruihong Liang³, Chen Liu⁴,
Yinchang Ma⁴, Xi-xiang Zhang⁴, Shiyang Wei⁵, Junwei Zhang⁶, Zhi Tan¹,
Zhipeng Wang⁶✉, Xiang Lv¹✉ & Jiagang Wu^{1,7}✉

Piezoceramics for high-power applications require both high piezoelectric coefficient (d_{33}) and mechanical quality factor (Q_m). However, the trade-off between them poses a significant challenge in achieving high values simultaneously, which is more prominent in lead-free piezoceramics. Here, we propose a new strategy, local Cu-acceptor defect dipoles embedded orthorhombic-tetragonal phase boundary engineering (O-T PBE), to balance d_{33} and Q_m in potassium sodium niobate piezoceramics. This is validated in $0.95(\text{K}_{0.48}\text{Na}_{0.52})\text{NbO}_3\text{-}0.05(\text{Bi}_{0.5}\text{Na}_{0.5})\text{HfO}_3\text{-}0.2\%\text{molFe}_2\text{O}_3\text{-}x\text{mol}\%\text{CuO}$ ceramics. Our strategy simultaneously maintains the O-T PBE and introduces local dimeric $(\text{Cu}_{\text{Nb}}'' - \text{V}_{\text{O}}'')$ and trimeric $(\text{V}_{\text{O}}'' - \text{Cu}_{\text{Nb}}'' - \text{V}_{\text{O}}'')$ defects. The dimeric defects form defect dipole polarization that pins domain wall motion, while the trimeric ones introduce the local structural heterogeneity that leads to nano-scale multi-phase coexistence and abundant nano-domains. Encouragingly, for the Cu-doped sample with $x = 1$, Q_m increases by a factor of 4, but d_{33} only decreases by 1/5 (i.e., achieving a d_{33} of 340 pC/N and a Q_m of 256). Our research provides a new paradigm for balancing d_{33} and Q_m in lead-free piezoceramics, which holds promise for high-power applications.

Piezoelectric materials interconvert electrical and mechanical energies and are widely used for sensors, actuators, transducers, and energy harvesters^{1–3}. These piezoelectric devices are crucial in various fields, including biomedical engineering, aerospace, and wireless energy transmission⁴. Piezoceramics, represented by lead zirconate titanate ($\text{Pb}(\text{Zr}, \text{Ti})\text{O}_3$, PZT) family, dominate the piezoelectric market due to

excellent electrical properties and large-scale industrial production⁵. Considering the toxicity of lead (Pb) and the need for environmental protection, research on lead-free piezoceramics to replace Pb-based ones is imperative⁶. Among these, potassium sodium niobate ((K, Na) NbO_3 , KNN)-based lead-free piezoceramics stand out due to the significant progress in their piezoelectric coefficient (d_{33}), electro-strain,

¹College of Materials Science and Engineering, Sichuan University, Chengdu 610065, China. ²Department of Materials Science and Engineering, Guangdong Provincial Key Laboratory of Materials and Technologies for Energy Conversion, Guangdong Technion-Israel Institute of Technology, Shantou 515063, China.

³Key Laboratory of Inorganic Functional Materials and Devices, Shanghai Institute of Ceramics, Chinese Academy of Sciences, Shanghai 201800, China.

⁴Division of Physical Science and Engineering, King Abdullah University of Science and Technology, Thuwal 23955-6900, Saudi Arabia. ⁵School of Materials and Energy and Electron Microscopy Centre, Lanzhou University, Lanzhou 730000, China. ⁶School of Advanced Materials and Nanotechnology, Xidian University, Xi'an 710126, China. ⁷College of Physics, Sichuan University, Chengdu 610065, China.

✉ e-mail: daniel.tan@gtit.edu.cn; wangzhipeng@xidian.edu.cn; lvxiang@scu.edu.cn; msewujg@scu.edu.cn

and temperature stability achieved through phase boundary engineering (PBE), texturing, defect engineering, and composite ceramics⁷.

For high-power applications such as ultrasonic motors, cleaners, and transducers, piezoceramics are expected to have both high d_{33} and mechanical quality factor (Q_m) (also known as hard piezoceramics) as they operate in resonant mode⁵. High d_{33} ensures the good electromechanical properties, while high Q_m reduces the heat generation caused by dissipated energy⁸. However, achieving a balance between d_{33} and Q_m is highly challenging because they have different preferences for extrinsic contributions. Specifically, high d_{33} prefers more ferroelectric domain switching, while high Q_m is usually achieved by pinning domain switching⁵. This imbalance is more pronounced in KNN-based piezoceramics. For example, although the PBE strategy significantly increases d_{33} to the level of 400–600 pC/N, it is accompanied by an extremely low Q_m (<50)^{9,10}. Traditional acceptor doping (i.e., copper Cu and manganese Mn) and the newly-proposed isolated-oxygen-vacancy strategy greatly improve Q_m but fail to ensure high d_{33} ^{5,11}. Additionally, traditional acceptor doping is mainly implemented on pristine KNN ceramics with low d_{33} values (e.g., <150 pC/N), resulting in even worse d_{33} after acceptor doping as expected.

It is known that the traditional orthorhombic-tetragonal (O-T) PBE reduces the energy barrier between O and T phases and promotes

domain switching, thereby enhancing dielectric and piezoelectric properties^{12,13}. However, the promoted domain switching also intensifies energy dissipation and seriously worsens Q_m (Fig. 1a). Here, we propose a new strategy to balance d_{33} and Q_m of KNN-based ceramics, namely, local Cu-acceptor defect dipoles embedded O-T PBE. Based on the O-T PBE, we innovatively embed local Cu-acceptor defect dipoles for two purposes. On the one hand, doping an appropriate Cu^{2+} has little effect on the phase transition temperature and can retain the room-temperature O-T PBE^{14,15}. On the other hand, the valence state difference between Cu^{2+} and Nb^{5+} provides a dual effect. Specifically, Cu-acceptor doping forms two defect configurations, namely, dimeric $(\text{Cu}_{\text{Nb}}'' - \text{V}_{\text{O}}^{\bullet\bullet})'$ and trimeric $(\text{V}_{\text{O}}^{\bullet\bullet} - \text{Cu}_{\text{Nb}}''' - \text{V}_{\text{O}}^{\bullet\bullet})^*$ ^{16–18}. The former primarily forms an electric dipole moment (i.e., defect dipoles, P_D) to pin domain switching in addition to a slight elastic distortion, whereas the latter mainly has an elastic distortion with no electric dipole. The local elastic distortion can cause the increased local structural heterogeneity, consequently further reducing the domain size and lowering the polarization energy barrier^{19,20}. That is to say, our strategy can construct a “flat and deep” potential well. The “flat” region is contributed by the retained O-T PBE and the introduced local structural heterogeneity, ensuring high d_{33} , while the “deep” wall comes from the dimeric P_D that prevents long-range polarization rotation and pins

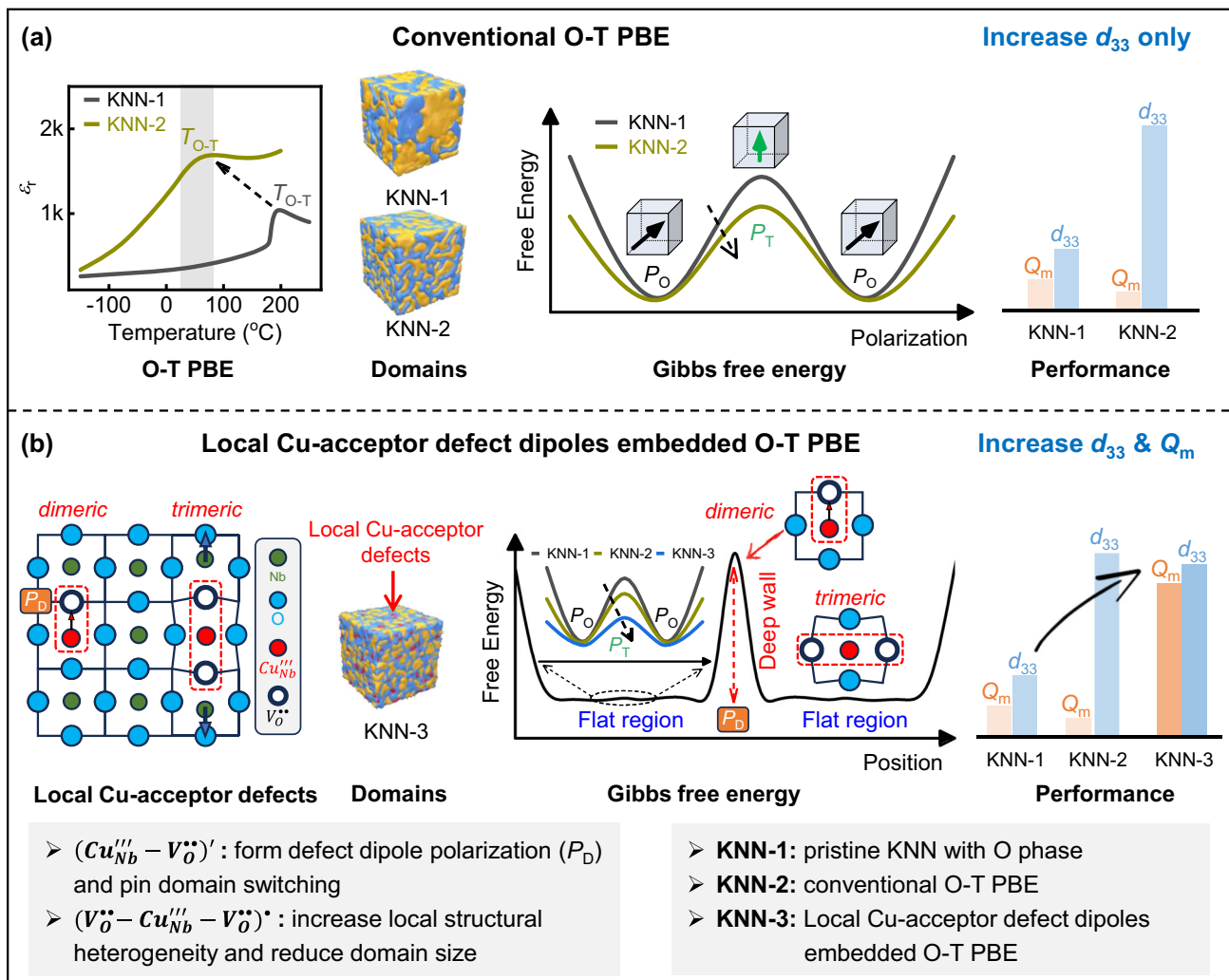


Fig. 1 | Schematic illustrations of conventional O-T PBE and our local Cu-acceptor defect dipoles embedded O-T PBE strategy. a For the conventional O-T PBE strategy, only d_{33} can be enhanced due to the easy polarization rotation and domain switching, leaving an unbalanced development of d_{33} and Q_m . **b** For our

local Cu-acceptor defect dipoles embedded O-T PBE strategy, both d_{33} and Q_m can be simultaneously improved because of the coupling effect of local Cu-acceptor defect dipoles and O-T PBE. Note that PBE is the abbreviation of phase boundary engineering.

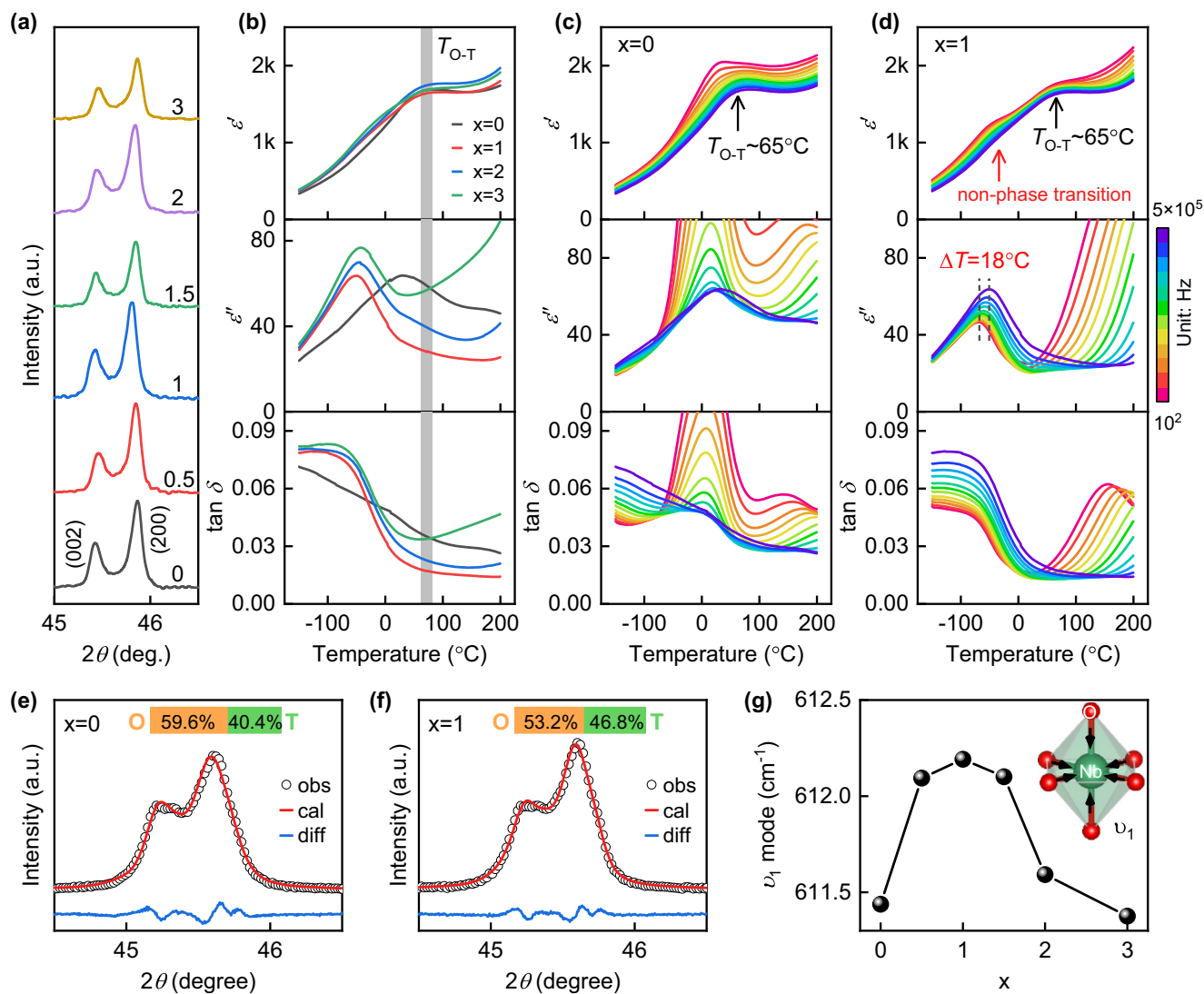


Fig. 2 | Phase structure study. **a** Enlarged view of XRD pattern with $2\theta = 45\text{--}46^\circ$. **b** $\varepsilon' - T$, $\varepsilon'' - T$, and $\tan \delta - T$ curves of unpoled samples, measured at 500 kHz. Frequency-dependent $\varepsilon' - T$, $\varepsilon'' - T$, and $\tan \delta - T$ curves of KNN-BNH- x Cu with (c) $x = 0$ and (d) $x = 1$. Enlarged view of Rietveld refinements for powder XRD patterns of KNN-BNH- x Cu

with (e) $x = 0$ and (f) $x = 1$. (g) Variations of ν_1 mode position with x . The insets of (e, f) show the phase fraction of O and T phases, and the inset of (g) is the schematic of ν_1 mode of NbO_6 octahedron.

adjacent domain wall motion (Fig. 1b). Besides, CuO, as the sintering aid, can enhance the sinterability and consequently improve density and grain size of KNN-based ceramics²¹. The appropriate increase in grain size can reduce the lattice stress caused by the domain switching, favoring piezoelectric properties²². Thus, both high d_{33} and Q_m are expected in such a system. We carefully select $0.95(\text{K}_{0.48}\text{Na}_{0.52})\text{NbO}_3 \cdot 0.05(\text{Bi}_{0.5}\text{Na}_{0.5})\text{HfO}_3 \cdot 0.2\% \text{molFe}_2\text{O}_3 \cdot x\% \text{molCuO}$ (abbreviated as KNN-BNH- x Cu) ceramics to implement our strategy because the KNN-BNH ceramic matrix exhibits the O-T PBE and high piezoelectricity^{23,24}. Encouragingly, KNN-BNH- x Cu ceramics successfully validate our strategy and exhibit balanced d_{33} (~ 340 pC/N) and Q_m (~ 256) at $x = 1.0$. Moreover, the related physical mechanisms are analyzed from the multi-scale perspective (i.e., local-mesoscopic-macroscopic) by using combined theoretical and experimental techniques.

Results and discussion

Phase structure

X-ray diffraction (XRD) patterns show that all samples have a typical perovskite structure. At high doping content, a minor CuO phase is observed (Supplementary Fig. 1), indicating that Cu^{2+} ions have entered into the lattice of KNN-BNH ceramic matrix. Enlarged XRD patterns in

the 2θ range of $45\text{--}46^\circ$ show the changes in position and relative intensity of $\{200\}_{\text{pc}}$ diffraction peaks with different doping levels (Fig. 2a). When $x = 0\text{--}1$, the diffraction peaks first shift a lower angle and then to a higher angle at $x = 1.5\text{--}3$. This can be explained by the replacement of Nb^{5+} ions (with a radius of 0.64 \AA when coordination number is 6) by Cu^{2+} ions (with a radius of 0.73 \AA when coordination number is 6) according to Bragg's Law ($2d\sin\theta = \lambda$)²⁵. As x ranges from 1.5 to 3, the diffraction peaks shift to a higher angle, which may be due to the existence of the secondary CuO phase affecting the lattice structure. The relative intensity of the $\{200\}_{\text{pc}}$ diffraction peaks also changes with x . For the undoped sample ($x = 0$), the intensity ratio of $(200)_{\text{pc}}$ to $(002)_{\text{pc}}$ peak is approximately 2:1, indicating the existence of the T phase¹⁰. As x increases, the I_{200}/I_{002} ratio first increases in the range of $x = 0\text{--}1$ but then changes irregularly in the range of $x = 1.5\text{--}3$. Thus, the sample with $x = 1$ seems to be a critical point.

To further study the phase structure, temperature-dependent dielectric properties (including ε' , ε'' , and $\tan \delta$) are analyzed. All samples show a dielectric anomaly near 65°C in their $\varepsilon' - T$ curves due to the O-T phase transition (i.e., $T_{\text{O-T}}$) (Fig. 2b), coinciding with their T-phase featured $\{200\}_{\text{pc}}$ diffraction peaks at room temperature. Notably, Cu-doped KNN-BNH ceramics show another weak dielectric

anomaly below the T_{O-T} in $\varepsilon''-T$ curves, which is more significant in the corresponding $\varepsilon'-T$ curves. Specifically, the $\varepsilon''-T$ curve of the undoped KNN-BNH ceramic shows an anomaly near T_{O-T} , while the $\varepsilon''-T$ curves of all Cu-doped KNN-BNH ceramics exhibit an anomaly near -50°C (much lower than their T_{O-T}). Obviously, these low-temperature anomalies of Cu-doped samples are not related to any phase transitions.

To further analyze the low-temperature anomalies, $\varepsilon'-T$ and $\varepsilon''-T$ curves are measured over a frequency range of 0.1–500 kHz (Fig. 2c, d and S2). The undoped KNN-BNH ceramic shows dielectric anomalies near T_{O-T} in both $\varepsilon'-T$ and $\varepsilon''-T$ curves, similar to canonical ferroelectric ceramics. The abnormally high ε'' and $\tan \delta$ values near T_{O-T} under low frequency can be attributed to space charges, as both values reduce sharply but do not shift with increasing frequency^{14,26}. In contrast, doping CuO gradually broadens the dielectric anomaly of T_{O-T} , especially at $x=2$ and 3 (Supplementary Fig. 2), indicating the enhanced degree of dielectric relaxation. All Cu-doped KNN-BNH ceramics exhibit an obvious dielectric anomaly near -50°C in their $\varepsilon'-T$ curves (especially under low frequencies). Importantly, these low-temperature anomalies are highly frequency-dependent in their $\varepsilon''-T$ curves, similar to the dielectric relaxation behavior of relaxor ferroelectrics^{27,28}. For example, at $x=1$, the temperature difference (ΔT) of the local maximum ε'' is about 18°C (Fig. 2d). Similar phenomena are also observed when comparing Cu-doped and Cu-undoped KNN ceramics (Supplementary Fig. 3). Meanwhile, Cu-doped KNN-BNH ceramics show higher $\tan \delta$ values at $T < -50^\circ\text{C}$ (far below T_{O-T}) (Fig. 2b), indicative of more local structural heterogeneities¹⁹. Therefore, these low-temperature anomalies are not related to phase transitions but inherently attributed to the addition of CuO, which disrupts the long-range ferroelectric order and induces more local structural heterogeneities.

Due to the highly close T_{O-T} values, Rietveld refinements are carried out for powder XRD patterns of ceramics with $x=0$ and 1 (Fig. 2e, f and S5, Supplementary Table 1). A combination of O and T phases can well describe the measured data, confirming the coexistence of O-T phases. Although the T_{O-T} values remain almost unchanged, the Rietveld refinements show a slight increase in the T phase content from 40.4% (at $x=0$) to 46.8% (at $x=1$), which is consistent with the variations in bulk XRD patterns. To further explore the influence of CuO on the lattice structure, structure-sensitive Raman spectra are studied (Supplementary Fig. 6)²⁹. The Lorentz function is used to fit the Raman peaks within $500\text{--}700\text{ cm}^{-1}$ to extract the ν_1 vibration mode that represents the double-degenerate symmetric O-Nb-O stretching vibration³⁰. As x increases, ν_1 first shifts to a higher wavenumber at $x=0\text{--}1$ and then to a lower wavenumber at $x=1.5\text{--}3$ (Fig. 2g). A shift of ν_1 to higher wavenumbers indicates the enhanced B-O bond energy³¹. Therefore, doping CuO enhances the Nb-O bond energy except for at high content (i.e., $x=3$). The detailed explanation will be discussed later. Moreover, the Raman spectra also prove that $x=1$ is a critical point.

Microscopic-mesoscopic-local structures

Multi-scale structural studies are then conducted to reveal the physical mechanisms. Both average grain size and relative density increase with x , well aligning with our expectation (Supplementary Fig. 7 and Supplementary Table 2). The excess CuO accumulates at the grain boundaries and causes the relative density exceeding 100% at $x=3$ due to its much larger density ($6.3\text{--}6.9\text{ g/cm}^3$) than KNN-BNH ceramic matrix (4.6 g/cm^3). Both SEM-EDS and TEM-EDS observations confirm uniform distribution of all elements in the KNN-BNH-1Cu sample, further proving that Cu atoms have completely entered the lattice of KNN-BNH matrix (Supplementary Fig. 8–11 and Supplementary Table 3). Subsequently, ferroelectric domains are studied by performing out-of-plane PFM (OP-PFM) measurements. The domain configurations highly depend on the content of CuO. The Cu-undoped sample (i.e., $x=0$) exhibit complex domain configurations containing

both small nano-sized domains ($\sim 170\text{ nm}$) and large micron-sized domains ($\sim 1\text{ }\mu\text{m}$) (Fig. 3a), akin to those of the reported ceramics with multi-phase coexistence^{32,33}. In contrast, the KNN-BNH-1Cu sample shows overwhelmingly high-density nano-sized domains with a size of $\sim 100\text{ nm}$ (Fig. 3b). These nano-sized domains have been reported to rapidly respond to external electric fields and thus enhance piezoelectricity³⁴. However, the KNN-BNH-3Cu sample displays the fragmented and isolated domains and much low-density domain walls (Fig. 3c), consistent with its increased degree of dielectric relaxation. The domain configurations are further confirmed in randomly selected different areas (Supplementary Fig. 12–14). Switching spectroscopy PFM (SS-FPM) measurements are performed on several random points to study local domain switching (Fig. 3 and Supplementary Fig. 15). All samples show amplitude loops with a typically butterfly shape and phase loops with a maximum phase-contrast of 180° , indicating sufficient local domain switching. It is noted that adding CuO makes the amplitude loops become asymmetrical, indicating the existence of local defect dipoles. Interestingly, as x increases, the local coercive voltage (i.e., $\Delta V_C = V + V_C - V_C$) decreases, while the maximum amplitude value increases. Thus, doping with CuO not only introduces the defect dipoles but also facilitates local domain switching, which is expected to maintain high d_{33} and improve Q_m simultaneously.

We further conduct TEM/STEM imaging for the KNN-BNH-1Cu sample to study the local structure. TEM images reveal multifarious ferroelectric domains, including irregular nano-domains of $\sim 50\text{ nm}$ (Fig. 4a), hierarchical nano-domains of $\sim 20\text{--}50\text{ nm}$ (Fig. 4b and Supplementary Fig. 16), and lamellar domains ranging from $200\text{--}400\text{ nm}$ (Supplementary Fig. 16). These nanodomains were widely reported in lead-free and lead-based piezoceramics with high piezoelectricity³⁵, indicating superior piezoelectric properties at $x=1$. Then the local atomic structure were studied using the STEM-HAADF measurements and simulating polarization vectors (Fig. 4c, d). The calculated polarization vectors show the coexisting R/O and T phases along the [100] direction, with an average polarization displacement of 27.0 pm (Fig. 4c–e). The [110]-orientated STEM HAADF image also shows the nanoscale coexistence of R, O, and T phases (Supplementary Fig. 18). The phase gradually transforms on the nanoscale, leading to abundant nano-domains and easy local domain switching. Interestingly, the local T phase mainly locates at the areas with more A-site atom intensity (Fig. 4f). This phenomenon may be rationalized by the large ionic radius of K^+ ions and remarkable off-center displacement of Bi^{3+} ions, building larger cube-octahedral cages that allow Nb^{5+} to displace along the [001] direction^{36,37}. Additionally, the c/a ratio and lattice parameter maps reveal distinctly local structural heterogeneities associated with the addition of these chemical dopants like BNH and CuO (Fig. 4g, h).

Electromechanical properties

As x increases in KNN-BNH- x Cu ceramics, d_{33} gradually decreases while Q_m first increases and then decreases, with optimal properties at $x=1$ (i.e., $d_{33}=340\text{ pC/N}$ and $Q_m=256$) (Fig. 5a). For KNN-based piezoceramics, a d_{33} higher than 300 pC/N is usually accompanied by a low Q_m value (e.g., <150). Thus, the balanced d_{33} and Q_m values obtained here are superior to those of previously-reported KNN-based ceramics (Fig. 5b)^{11,38–43}. The hardening of piezoceramics increases the phase angle, which is also observed in these samples. The KNN-BNH-1Cu sample shows a higher phase angle of 86.7° compared to the KNN-BNH sample (Fig. 5c, d), indicating a more saturated poling process⁴⁴. This increased phase angle is also observed for other Cu-doped KNN-BNH samples even at the high doping content (Supplementary Fig. 20). A radar map is used to compare the electrical properties between KNN-BNH-0CuO and KNN-BNH-1CuO samples (Fig. 5e). The KNN-BNH-1CuO sample has a d_{33} value only decreasing by 1/5 but a Q_m increasing by a factor of 4, proving much better overall performance.

The hardening effect stems from the defect dipoles studied by $P-E$ loops of unpoled samples under the first two electric cycles. The KNN-

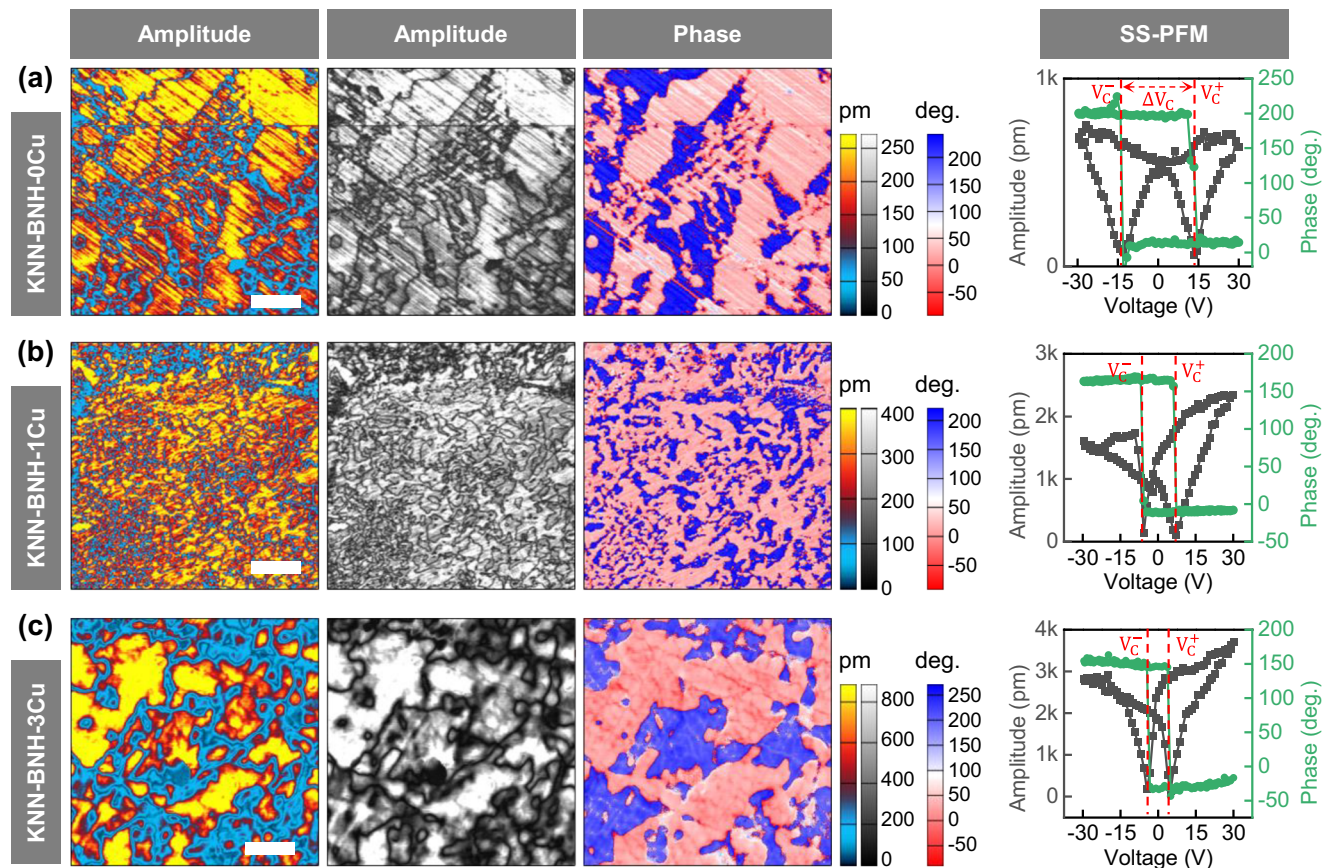


Fig. 3 | Mesoscopic ferroelectric domain structure. Amplitude and phase images of OP-FPM measurements and SS-PFM measurements of (a) KNN-BNH-0Cu, (b) KNN-BNH-1Cu, and (c) KNN-BNH-3Cu ceramics. The scanning area of is $5 \mu\text{m} \times$

$5 \mu\text{m}$, and the white bars represent $1 \mu\text{m}$. For a better view, the amplitude images are shown with colorful and gray, respectively.

BNH-0Cu ceramics show highly similar P - E loops under two electric cycles (Supplementary Fig. 19). By contrast, the Cu-doped KNN-BNH ceramics with $x = 0.5$ – 1.5 show the decreased maximum polarization (P_{max}) during the second electric cycle (Fig. 5f and Supplementary Fig. 19), which can be explained by the dynamic activities of defect dipoles. Taking the KNN-BNH-1Cu ceramic as an example (Fig. 5f–h):

- At point *a*: ferroelectric domains and defect dipoles randomly distribute in the unpoled state, and defect dipoles align with the direction of domains according to the symmetry-conforming principle⁴⁵;
- At point *b*: applying a positive electric field of $+30 \text{ kV/cm}$ drives the most domains upwards, except for a few domains close to defect dipoles because orientations of these defect dipoles differ from the electric field;
- At point *d*: applying a negative electric field of -30 kV/cm makes some domains downwards, but defect dipoles pin the switching of their adjacent domains, resulting in the smaller P_{max} than that measured at point *b*;
- At point *f*: applying a positive electric field of $+30 \text{ kV/cm}$ again makes less domains upwards due to the pinning of defect dipoles, resulting in much smaller P_{max} than that measured at point *b*.
- At point *h*: Since the pinning effect of defect dipoles gets saturated, the unpinned domains can rapidly switch under external electric fields, resulting in the almost equal P_{max} values at points *f* and *h*.

For Cu-doped KNN-BNH ceramics with $x = 2$ – 3 , the first two P - E loops highly overlap due to the enhanced dielectric relaxation behavior offsetting the pinning effect of doping CuO.

Formation mechanisms of defect dipoles

X-ray absorption fine structure (XAFS) spectra measurements and the first-principle calculations are further used to reveal the formation mechanism of Cu-related defect dipoles. Cu K -edge and Nb K -edge XAFS measurements (Fig. 6a–c and Supplementary Fig. 21) show that the rising edge position for the Cu K -edge X-ray absorption near edge spectra (XANES) of Cu-doped KNN-BNH samples is closer to that of CuO reference (Fig. 6a), indicating the same valence state (i.e., $+2$). Cu-doped KNN-BNH samples also show a shoulder peak at 8986 eV ($1s$ to $4p_z$ transition), suggesting a similar square planar coordination environment as CuO (Fig. 6a)^{46,47}. Fig. 6b, c presents the k^2 -weighted Cu K -edge Fourier transform EXAFS (FT-EXAFS) spectra and their EXAFS fitting results in R space. For Cu-doped KNN-BNH samples, there is a sharp peak at $R \sim 1.5 \text{ \AA}$, corresponding to the Cu-O coordination shell. Lack of distinctly sharp peak at $R > 2 \text{ \AA}$ indicates that Cu atoms in Cu-doped KNN-BNH samples have no long-range order in the crystal lattice, unlike the situation of Nb atoms (Supplementary Fig. 21b). Furthermore, the EXAFS fitting results suggest that the Cu atoms in Cu-doped KNN-BNH samples have a coordination number (CN) of 3.8 – 4.1 , and the average Cu-O bond length is around 1.93 \AA (Fig. 6c and Supplementary Table 4). These results confirm that the Cu atoms in Cu-doped KNN-BNH samples possess the CuO_4 square planar coordination structure, which unambiguously proves the existence of the trimeric $(V_{\text{O}}^{\bullet\bullet} - \text{Cu}_{\text{Nb}}^{\prime\prime} - V_{\text{O}}^{\bullet\bullet})^{\bullet}$ defect configuration¹⁶.

Considering the proven Cu-O square planar structure, the first-principles calculations based on density functional theory (DFT) are used to calculate the local crystal structure of Cu-doped KNN (Fig. 6d–f and Supplementary Fig. 22)^{48,49}. The relaxed KNN-Cu supercells show that the oxygen vacancies form at the two top positions of the oxygen octahedron along the c axis, resulting in the Cu-O square planar

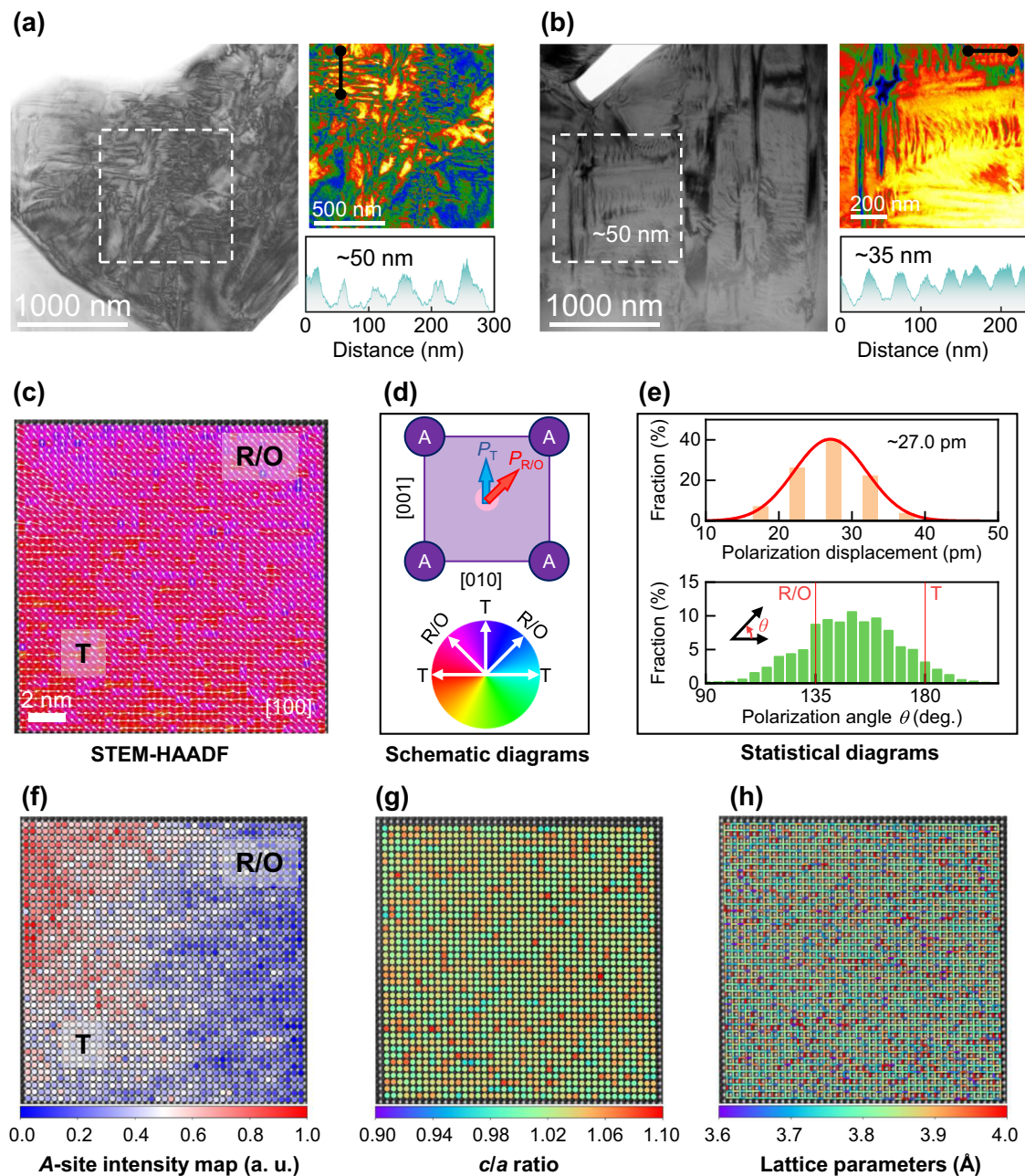


Fig. 4 | Mesoscopic and atomic scale study of KNN-BNH-1Cu ceramics. a, b TEM images of KNN-BNH-1Cu ceramics. **c** STEM-HAADF image along the [100] direction, covered by simulated polarization vectors. **d** Schematic diagrams of the ABO₃ unit cell along the [100] zone axis and the color wheel of simulated polarization vectors

in (c). **e** Statistical diagrams of polarization displacement and angle of simulated polarization vectors in (c). **(f-h)** A-site atom intensity map, *c/a* ratio map, and lattice parameters maps corresponding to (c). The statistics of domain size in (a, b) is along the black line segments.

structure within the *a-b* plane. This structure drives the Nb⁵⁺ closer to O²⁻ along the *c* (or -*c*) axis (as marked by the black arrows in Fig. 6d), enhancing Nb-O bond hybridization (Fig. 6e) and showing an elongation along the *c* axis (Supplementary Fig. 22). Compared to the pristine KNN supercells, doping Cu atom significantly affects the Nb-O bond length of nearest and next-nearest NbO₆ octahedron (Fig. 6f and Supplementary Fig. 22), accounting for the observed local structural heterogeneities. Thus, the DFT calculations well explain the increased T phase content and the Raman ν_1 vibration shifting to higher wavenumber after adding CuO. Furthermore, the simulated theoretical Cu *K*-edge XANES spectra of relaxed KNN-Cu supercells are compared with the experimental spectra of KNN-BNH-1Cu sample (Fig. 6g). The simulated spectrum matches well with the experimental spectra, further proving the reliability of the DFT calculations.

The X-band electron paramagnetic resonance (EPR) spectra also show a stronger signal at $g=2.003$ for the KNN-BNH-1Cu sample, confirming more oxygen vacancies (Fig. 6h). Similar evidence is observed in the X-ray photoelectron spectra (XPS) (Supplementary Fig. 23). Temperature-dependent synchrotron XRD for the KNN-BNH-1Cu powder sample from -100 to 25 °C shows that as the temperature decreases, {110} diffraction peaks gradually transform from the T-phase feature to the O-phase one, and both {200} and {211} diffraction peaks also show the increased O phase content (as evidenced by the increased intensity of the left peak), as shown in Fig. 6i. Therefore, the low-temperature dielectric relaxation behavior in $\epsilon''-T$ curves is due to the local structural heterogeneity rather than global phase transition, akin to the situations of relaxor ferroelectrics²⁷. Specifically, the KNN-BNH matrix is dominated by the O phase at low temperatures,

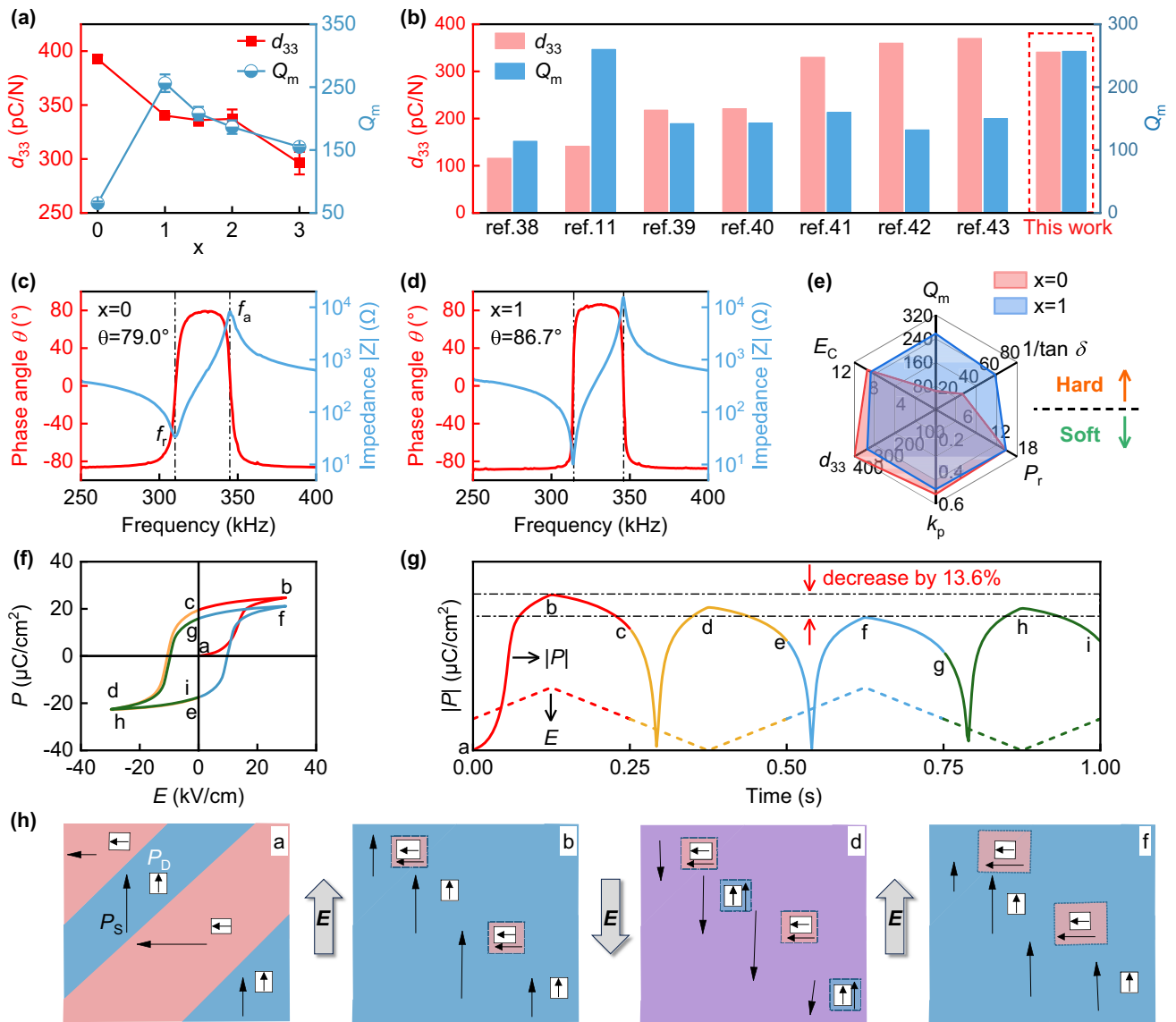
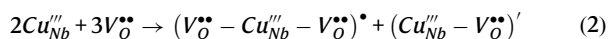
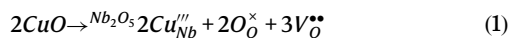


Fig. 5 | Electromechanical properties. **a** Variations of d_{33} and Q_m values with x . The error bar represents the standard deviation. **b** Comparison of d_{33} and Q_m values between this work and other reported KNN-based ceramics. Frequency-dependent phase angle and impedance spectra of poled **(c)** KNN-BNH-0Cu and **(d)** KNN-BNH-1Cu ceramics. **e** Comparison of comprehensive properties of KNN-BNH-0Cu and KNN-

BNH-1Cu ceramics. **f** P - E loops and **(g)** polarization values of unpoled KNN-BNH-1Cu under the first two electric cycles. **h** Schematic diagrams showing domains and defect dipoles corresponding to different points in **(f)**. f_a and f_r in **(c)** are the anti-resonance and resonance frequencies, respectively. P_s and P_D in **(h)** represent the spontaneous polarization and the defect dipole polarization, respectively.

while the defect dipoles constrain the adjacent lattice cells with the T-phase feature.

Since the foregoing results and analysis unambiguously prove the existence of trimeric $(V_O^{**} - Cu_{Nb}'' - V_O^{**})^{\bullet}$ defect complex, the equal dimeric $(Cu_{Nb}'' - V_O^{**})'$ defect should also be observed to keep the electroneutrality condition according to the Kröger-Vink notation⁵⁰:



The dimeric ones establish P_D and cause an elastic distortion, while the trimeric ones only cause an elastic distortion¹⁶. Both dimeric and trimeric defects can hinder the domain switching, especially the dimeric ones due to the generated P_D . According to the principle of symmetry-conforming property of point defects, P_D aligns with the spontaneous

polarization (P_s) and restrains adjacent domain switching, achieving overall hardening effect (called as bulk effect)⁵¹. Meanwhile, the propagation of new domain walls during polarization process will be impeded by P_D , causing the hardening effect at domain walls (called as domain wall effect)^{52,53}. Both effects contribute to the hardening effect of KNN-BNH-Cu ceramics. The elastic distortion caused by both defects (especially the trimeric ones) induces the local structure heterogeneities that disturb the long-range ordering and decrease domain sizes, consequently flattening the energy barrier of the retained O-T PBE. Finally, as we designed, both d_{33} and Q_m can be enhanced via the local Cu-acceptor defect dipoles embedded O-T PBE strategy.

In this work, we propose the local Cu-acceptor defect dipoles embedded O-T PBE strategy to balance the development of d_{33} and Q_m of KNN-based ceramics and validate it with KNN-BNH- x CuO ceramics. This strategy retains the room-temperature O-T PBE in KNN-BNH- x Cu ceramics but introduces considerable Cu^{2+} -related defects, namely, dimeric $(Cu_{Nb}'' - V_O^{**})'$ and trimeric $(V_O^{**} - Cu_{Nb}'' - V_O^{**})^{\bullet}$ defects. The retained

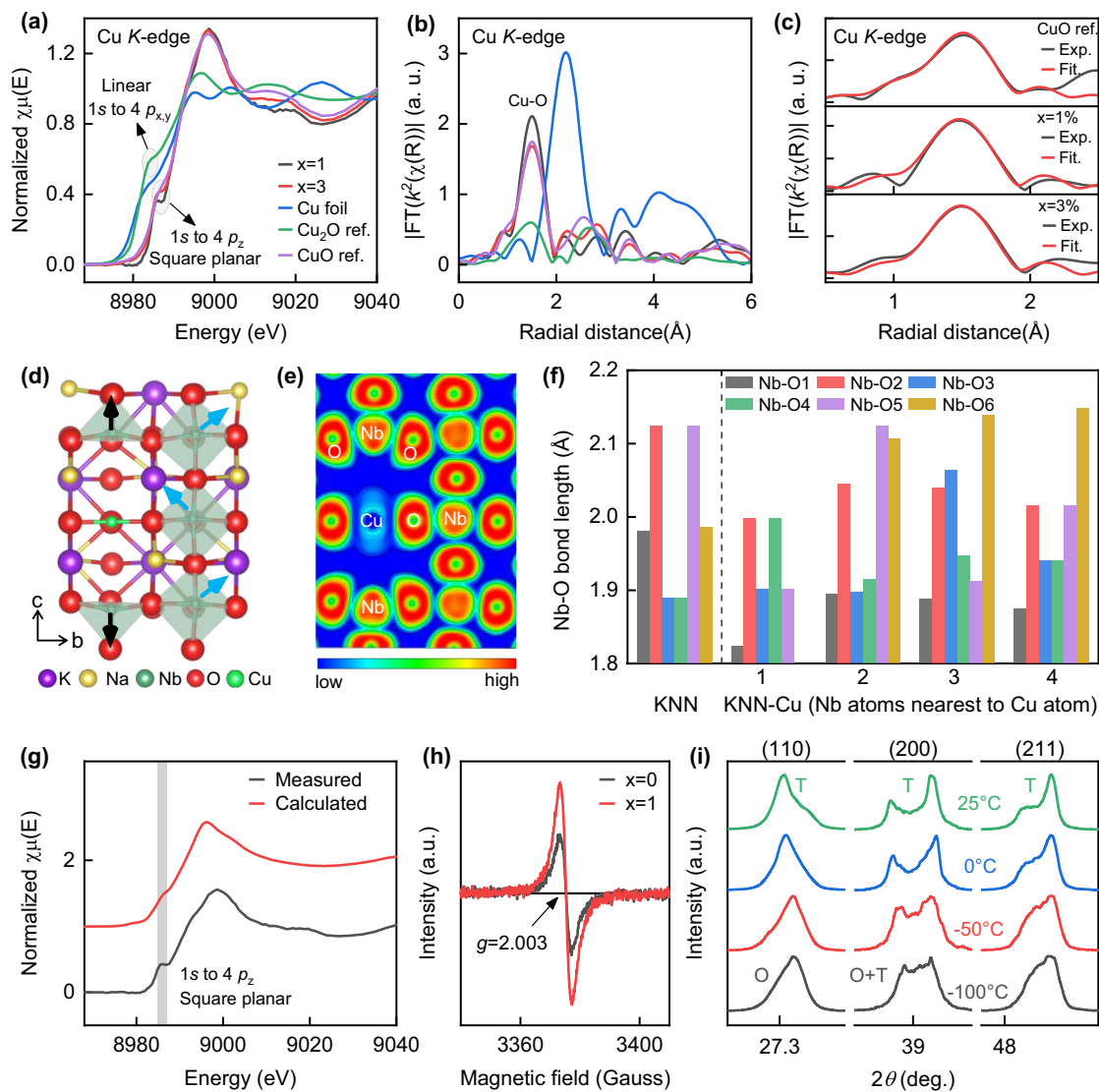


Fig. 6 | Formation mechanisms of defect dipoles. **a** Normalized Cu *K*-edge XANES spectra and **b** k^2 -weighted Cu *K*-edge FT-EXAFS spectra of KNN-BNH-Cu and standard samples (Cu foil, CuO, and Cu₂O). **c** Experimental and fitting FT-EXAFS spectra for KNN-BNH-Cu samples and CuO standard sample. **d** Lattice structure and **e** charge

density profiles of relaxed KNN-Cu supercells. **f** Comparisons of Nb-O bond lengths of relaxed KNN and KNN-Cu supercells. **g** Experimental and simulated Cu *K*-edge XANES spectra for the KNN-BNH-1Cu sample. **h** X-band EPR spectra of KNN-BNH-*x*Cu samples. **i** Synchrotron based XRD patterns of KNN-BNH-1Cu from -100 to 25 °C.

O-T PBE is featured with nanoscale multi-phase coexistence and abundant nano-domains due to the introduced local structural heterogeneities, ensuring high d_{33} . The trimeric $(V_{\text{O}}^{\bullet\bullet} - Cu_{\text{Nb}}^{\prime\prime} - V_{\text{O}}^{\bullet\bullet})^{\bullet}$ defect is unambiguously proved by the XAFS spectra showing the existence of CuO₄ square planar coordination structure. Such trimeric defect enhances the Nb-O bond energy and enhances the T phase characteristics, as proved by XRD patterns, Raman spectra, low-temperature synchrotron XRD patterns, and DFT calculations. The corresponding dimeric $(Cu_{\text{Nb}}^{\prime\prime} - V_{\text{O}}^{\bullet\bullet})^{\bullet}$ defect forms P_{D} that pins domain switching through the bulk and domain wall effects. Due to the coupling effect of the O-T PBE and the Cu²⁺-related defect configurations, the KNN-BNH-1Cu sample shows a combination of $d_{33} = 340$ pC/N and $Q_{\text{m}} = 256$, surpassing the results of other typical KNN-based piezoceramics. Therefore, our strategy provides a paradigm for simultaneously optimizing d_{33} and Q_{m} of lead-free piezoceramics that are promising for high-power applications.

Methods

Preparation of ceramics

0.95(K_{0.48}Na_{0.52})NbO₃-0.05(Bi_{0.5}Na_{0.5})HfO₃-0.2%molFe₂O₃-*x*%molCuO (KNN-BNH-*x*Cu; *x* = 0, 0.5, 1, 1.5, 2, and 3), K_{0.48}Na_{0.52}NbO₃-0.2%

molFe₂O₃ (KNN), and K_{0.48}Na_{0.52}NbO₃-0.2%molFe₂O₃-1%molCuO (KNN-1Cu) ceramics were synthesized by the conventional solid-state reaction method. High-purity raw materials of K₂CO₃ (99%), Na₂CO₃ (99.8%), Bi₂O₃ (99.999%), HfO₂ (99%), Fe₂O₃ (99.9%), Nb₂O₅ (99.95%), and CuO (99%) were purchased from the Sinopharm Chemical Reagent Co., Ltd (China). The small amount of Fe₂O₃ was added to improve the sinterability of ceramics. First, with the purpose of keeping the phase boundary feature, the calcinated KNN-BNH powder was prepared in advance. The raw materials were weighed according to stoichiometric ratio and mixed well with alcohol as medium in zirconia vessel at a speed of 258 r/min on the planetary ball mill for 12 h. The slurries were then dried and calcinated at 850 °C for 6 h. Then, the CuO was added into the calcinated KNN-BNH powder for the secondary ball milling. After secondary ball milling, the powder was bonded by 5 wt.% polyvinyl alcohol (PVA) and then pressed into disks (diameter: 10 mm, thickness: 1 mm) under a pressure of ~300 MPa. The organic PVA was burned at 600 °C for 4 h, and the green disks were sintered at 1070–1090 °C for 3 h. The sintered pellets were spread with silver paste on both sides and then were heated at 600 °C for 30 min to form the electrodes. Finally,

the samples were poled in the silicon oil at a direct current electric field of 3 kV/mm for 30 min.

Measurements for structure and performance

The density of ceramics was measured by the Archimedes method. For each composition, five ceramic disks were measured and the average density was calculated. The crystal structure of sintered ceramics was measured by an X-ray diffraction (XRD) equipment (Bruker D8 Advance XRD, Bruker AXS Inc., Madison, WI, Cu K_{α}). To conduct the Rietveld refinements, the as-sintered ceramics were manually ground into powder and then annealed at 600 °C for 2 h. The powder XRD (PXRD) patterns were collected by using a high-resolution XRD equipment (Empyrean, PANalytical, Netherlands), and the MAUD software was used for conducting the Rietveld refinements. Temperature-dependent synchrotron based XRD patterns were measured by the synchrotron X-ray beam (BL02U2 station of Shanghai Synchrotron Radiation Facility (SSRF)). Raman spectra were measured to study the local vibration modes of NbO₆ octahedron (LabRAM HR Evolution micro-Raman spectrometer, HORIBA Jobin-Yvon, France). To observe the ferroelectric domains, the as-sintered ceramics were polished mechanically (DS001, Truer, Shanghai, China). Then, the domain structures of polished ceramics were characterized by a piezoresponse force microscopy (PFM, MFP-3D, Asylum Research, Goleta, CA, USA) with a conductive Pt-Ir-coated cantilever (PPP-NCHPt, Nanosensors, Switzerland) in the contact mode. The microtopography of samples is collected by scanning electron microscope (SEM, GeminiSEM, ZEISS300, Germany). Transmission electron microscopy (FEI Titan Themis G2 300, Thermofisher Scientific) with a probe corrector was used to observe the microstructures at 300 kV.

The real part of the dielectric constant (ϵ'), the imaginary part of the dielectric constant (ϵ''), and dielectric loss ($\tan \delta$) were tested by a broadband dielectric spectrometer (Novocontrol Concept 80, Novocontrol Technologies GmbH, Germany) under the temperature from -150 to 200 °C at frequencies ranging from 0.1 to 500 kHz. A ferroelectric analyzer (aixACCT TF Analyzer 2000, Germany) was used to measure the polarization-electric field hysteresis loops (P - E) and strain-electric field curves (S - E) at room temperature. Electron paramagnetic resonance spectra (EPR, Bruker, Emxplus, Germany) and X-ray photoelectron spectra (XPS, XPS-ultracold, Kratos, England) were measured to study the oxygen vacancies. The piezoelectric coefficients (d_{33}) and mechanical quality factor (Q_m) were detected by a Berlincourt meter (ZJ-3A, Institute of Acoustics, Chinese Academy of Sciences) and an Impedance analyzer (Model PV70A Co., Ltd., Bandera Electronics, China), respectively. The mechanical quality factor (Q_m) was calculated by the resonance-antiresonance method according to the following formula⁵⁴:

$$Q_m \approx \frac{f_a^2}{2\pi f_r Z_r C^T (f_a^2 - f_r^2)} \quad (3)$$

To reveal the reliability of measured performance, we measured d_{33} and Q_m values of samples from different batches for each composition, and calculated the mean value and standard deviation (see Supplementary Tables 5-9). The small standard deviation manifests the stable performance from batch to batch and reliable measurements.

The Cu K -edge and Hf L_{3} -edge X-ray absorption fine structure (XAFS) spectra, including X-ray absorption near edge spectra (XANES) and extended X-ray absorption fine structure (EXAFS), were collected at XAFCA beamline of Singapore synchrotron light source (SSLS)⁵⁵. The Nb K -edge XAFS spectra were collected at the XAS beamline of Australian Synchrotron. For energy calibration, the Cu foil and Nb foil were measured simultaneously with the samples. All the data were processed according to the standard procedures in Athena module within the Demeter software packages. The EXAFS fitting was conducted by

Artemis software using FEFF6 theoretical scattering path calculation code⁵⁶. The Cu K -edge XANES spectra for the relaxed structural model of the KNN-BNH-1Cu sample was also simulated by the FDMNES software⁵⁷.

Atomic-resolution STEM image analysis

The atom positions were determined using a two-dimensional Gaussian peak-fitting method before calculating the atom displacement, the c/a ratio, and the lattice parameters. For the image along with the [100] zone axis, the displacement of the B-site atom in a perovskite structure was defined as the difference between its real position and the reference site based on the nearest four A-site atoms. For the image along with the [110] zone axis, the B-site atom displacement was obtained by calculating the difference between its real position and the averaged position of the two neighboring A-site atoms. The peak intensities of both A- and B-sites atoms were defined as the averaged intensity within an adaptive mask of each column, where the center of the mask is the position of the atom column and the radius is the full width at half maximum.

First principles calculations

The first-principle calculations are conducted based on density functional theory (DFT) as implemented in Vienna Ab initio Simulation Package (VASP)^{58,59}. The Perdew-Burke-Ernzerhof revised for solids (PBEsol)⁶⁰ exchange-correlation functional with projector-augmented wave (PAW)⁶¹ is employed. The Cu $3p^6 4s^3 3d^0$, K $3s^2 3p^6 4s^1$, Nb $4p^6 5s^2 4d^5$, and O $2s^2 2p^4$ orbitals are treated as valence electrons for calculations. A plane wave expansion with a cut-off energy of 520 eV is used to represent the wave function. Γ -centered k -point meshes with a grid of spacing $0.04 \times 2\pi \text{ \AA}^{-1}$ are selected for Brillouin zone sampling. The Kohn-Sham orbitals are iteratively updated in the self-consistency cycle until an energy convergence of 10^{-4} eV is obtained, and geometry optimizations proceed until the residual atomic forces are below 0.01 eV/Å. We select a $4 \times 4 \times 4$ perovskite supercell containing 320 atoms, with [111]-oriented K/Na ordering and [110] polarization as the initial structure. A Nb atom is then replaced by a Cu atom, and two adjacent oxygen atoms are removed to maintain a Cu-centered parallelogram configuration. After full relaxation, a stable Cu-doped KNN supercell is obtained.

Data availability

The authors declare that the data that support the findings of this study are available within the paper and its Supplementary Information files. More relevant data sets generated during and/or analyzed during the current study are available from the first authors and corresponding authors on reasonable request. Source data are provided with this paper.

References

- Jaffe B., Cook W. R., Jaffe H. *Piezoelectric Ceramics*. Academic Press (1971).
- Lv, X., Zhu, J., Xiao, D., Zhang, X.-x & Wu, J. Emerging new phase boundary in potassium sodium-niobate based ceramics. *Chem. Soc. Rev.* **49**, 671-707 (2020).
- Xu, Q. et al. Highly Flexible, High-Performance, and Stretchable Piezoelectric Sensor Based on a Hierarchical Droplet-Shaped Ceramics with Enhanced Damage Tolerance. *Adv. Mater.* **36**, 2311624 (2024).
- Li J.-F. *Lead-Free Piezoelectric Materials*. John Wiley & Sons (2021).
- Chen, L., Liu, H., Qi, H. & Chen, J. High-electromechanical performance for high-power piezoelectric applications: Fundamental, progress, and perspective. *Prog. Mater. Sci.* **127**, 100944 (2022).
- Leng, H. et al. Design and development of high-power piezoelectric ceramics through integration of crystallographic texturing and acceptor-doping. *Acta Mater.* **206**, 116610 (2021).

7. Leng, H. et al. High performance high-power textured Mn/Cu-doped PIN-PMN-PT ceramics. *Acta Mater.* **234**, 118015 (2022).
8. Xiao, W. et al. Well-balanced performance achieved in PZT piezoceramics via a multiscale regulation strategy. *Mater. Horiz.* **11**, 5285–5294 (2024).
9. Shi, H., Chen, J., Wang, R. & Dong, S. Full set of material constants of $(\text{Na}_{0.5}\text{K}_{0.5})\text{NbO}_3\text{-BaZrO}_3\text{-(Bi}_{0.5}\text{Li}_{0.5})\text{TiO}_3$ lead-free piezoelectric ceramics at the morphotropic phase boundary. *J. Alloy. Compd.* **655**, 290–295 (2016).
10. Rubio-Marcos, F. et al. Lead-Free Piezoceramics: Revealing the Role of the Rhombohedral–Tetragonal Phase Coexistence in Enhancement of the Piezoelectric Properties. *ACS Appl. Mater. Interfaces* **7**, 23080–23088 (2015).
11. Liu, Y. X. et al. Isolated-Oxygen-Vacancy Hardening in Lead-Free Piezoelectrics. *Adv. Mater.* **34**, 2202558 (2022).
12. Wu, J., Xiao, D. & Zhu, J. Potassium–Sodium Niobate Lead-Free Piezoelectric Materials: Past, Present, and Future of Phase Boundaries. *Chem. Rev.* **115**, 2559–2595 (2015).
13. Fu, J., Zuo, R. & Xu, Z. High piezoelectric activity in $(\text{Na,K})\text{NbO}_3$ based lead-free piezoelectric ceramics: Contribution of nanodomains. *Appl. Phys. Lett.* **99**, 062901 (2011).
14. Cangini, L. et al. Hardening of $\text{K}_{0.5}\text{Na}_{0.5}\text{NbO}_3$ piezoceramics with Cu and the temperature dependence in high-power drive. *J. Materiomics.* **11**, 100962 (2025).
15. Han, H.-S. et al. Hardening behavior and highly enhanced mechanical quality factor in $(\text{K}_{0.5}\text{Na}_{0.5})\text{NbO}_3$ -based ceramics. *J. Eur. Ceram. Soc.* **37**, 2083–2089 (2017).
16. Eichel, R.-A. et al. Interactions of defect complexes and domain walls in CuO-doped ferroelectric $(\text{K,Na})\text{NbO}_3$. *Appl. Phys. Lett.* **102**, 242908 (2013).
17. Eichel, R.-A. et al. Local variations in defect polarization and covalent bonding in ferroelectric Cu^{2+} -doped PZT and KNN functional ceramics at the morphotropic phase boundary. *Phys. Chem. Chem. Phys.* **11**, 8698–8705 (2009).
18. Wu, Y. et al. KNN-Based Lead-Free Piezoelectric Ceramics with High Q_m and Enhanced d_{33} via a Donor–Acceptor Codoping Strategy. *Inorg. Chem.* **62**, 15094–15103 (2023).
19. Li, F. et al. Ultrahigh piezoelectricity in ferroelectric ceramics by design. *Nat. Mater.* **17**, 349–354 (2018).
20. Li, C. et al. Atomic-scale origin of ultrahigh piezoelectricity in samarium-doped PMN-PT ceramics. *Phys. Rev. B* **101**, 140102 (2020).
21. Chen, K. et al. Screening Sintering Aids for $(\text{K}_{0.5}\text{Na}_{0.5})\text{NbO}_3$ Ceramics. *J. Am. Ceram. Soc.* **98**, 1698–1701 (2015).
22. Zhang, M.-H. et al. Understanding the grain size dependence of functionalities in lead-free $(\text{Ba,Ca})(\text{Zr,Ti})\text{O}_3$. *Acta Mater.* **276**, 120112 (2024).
23. Chen, Y. et al. Effects of $\text{Bi}_{0.5}\text{Na}_{0.5}\text{HfO}_3$ addition on the phase structure and piezoelectric properties of $(\text{K, Na})\text{NbO}_3$ -based ceramics. *J. Am. Ceram. Soc.* **100**, 3920–3927 (2017).
24. Zhang, J., Sun, X., Su, W., Yao, W. & Zhou, C. Superior piezoelectricity and rhombohedral-orthorhombic-tetragonal phase coexistence of $(1-x)(\text{K,Na})(\text{Nb,Sb})\text{O}_3\text{-x}(\text{Bi,Na})\text{HfO}_3$ ceramics. *Scr. Mater.* **176**, 108–111 (2020).
25. Shannon, R. D. Revised effective ionic radii and systematic studies of interatomic distances in halides and chalcogenides. *Acta Crystallogr. Sect. A* **32**, 751–767 (1976).
26. Gomes, M. M. et al. Revisiting the phase sequence and properties of $\text{K}_{0.5}\text{Na}_{0.5}\text{NbO}_3$ ceramics sintered by different processes. *Ceram. Int.* **47**, 8308–8314 (2021).
27. Li, F. et al. The origin of ultrahigh piezoelectricity in relaxor-ferroelectric solid solution crystals. *Nat. Commun.* **7**, 13807 (2016).
28. Bokov, A. A. & Ye, Z. G. Recent progress in relaxor ferroelectrics with perovskite structure. *J. Mater. Sci.* **41**, 31–52 (2006).
29. Rubio-Marcos, F., Bañares, M. A., Romero, J. J. & Fernandez, J. F. Correlation between the piezoelectric properties and the structure of lead-free KNN-modified ceramics, studied by Raman Spectroscopy. *J. Raman Spectrosc.* **42**, 639–643 (2011).
30. Peddigari, M. & Pamu, D. Raman and Dielectric Studies on Lead free $(\text{K}_{0.5}\text{Na}_{0.5})\text{NbO}_3$ Piezoelectric Ceramics. *IOP Conf. Ser.: Mater. Sci. Eng.* **73**, 012141 (2015).
31. Schütz, D. et al. Lone-Pair-Induced Covalency as the Cause of Temperature- and Field-Induced Instabilities in Bismuth Sodium Titanate. *Adv. Funct. Mater.* **22**, 2285–2294 (2012).
32. Liu, Q., Pan, E., Deng, H., Liu, F. & Li, J.-F. Dy^{3+} doped $(\text{K,Na})\text{NbO}_3$ -based multifunctional ceramics for achieving enhanced temperature-stable piezoelectricity and non-contact optical temperature sensing performance. *Inorg. Chem. Front.* **10**, 2359–2369 (2023).
33. Yao, W. et al. High piezoelectric performance and domain configurations of $(\text{K}_{0.45}\text{Na}_{0.55})_{0.98}\text{Li}_{0.02}\text{Nb}_{0.76}\text{Ta}_{0.18}\text{Sb}_{0.06}\text{O}_3$ lead-free ceramics prepared by two-step sintering. *J. Eur. Ceram. Soc.* **39**, 287–294 (2019).
34. Tao, H., Yin, J., Zhao, C. & Wu, J. Relaxor behavior of potassium sodium niobate ceramics by domain evolution. *J. Eur. Ceram. Soc.* **41**, 335–343 (2021).
35. Lv, X., Zhang, X.-x & Wu, J. Nano-domains in lead-free piezoceramics: a review. *J. Mater. Chem. A* **8**, 10026–10073 (2020).
36. Lv, X., Zhang, N., Ma, Y., Zhang, X.-x & Wu, J. Coupling effects of the A-site ions on high-performance potassium sodium niobate ceramics. *J. Mater. Sci. Technol.* **130**, 198–207 (2022).
37. Levin, I. et al. Coupling of emergent octahedral rotations to polarization in $(\text{K,Na})\text{NbO}_3$ ferroelectrics. *Sci. Rep.* **7**, 15620 (2017).
38. Ling, P. et al. Structure and piezoelectric properties of $\text{K}_{0.5}\text{Na}_{0.5}\text{NbO}_3\text{-AlFeO}_3$ lead-free ceramics by using AlFeO_3 as a sintering aid. *J. Mater. Sci. -Mater. Electron.* **25**, 323–327 (2014).
39. Liao, Y. et al. Transformation of hardening to softening behaviors induced by Sb substitution in CuO-doped KNN-based piezoceramics. *Ceram. Int.* **45**, 13179–13186 (2019).
40. Jiang, X. P., Chen, Y., Lam, K. H., Choy, S. H. & Wang, J. Effects of MnO doping on properties of $0.97\text{K}_{0.5}\text{Na}_{0.5}\text{NbO}_3\text{-}0.03(\text{Bi}_{0.5}\text{K}_{0.5})\text{TiO}_3$ piezoelectric ceramics. *J. Alloy. Compd.* **506**, 323–326 (2010).
41. Li, H. et al. Hardening Effect on the Electromechanical Properties of KNN-Based Ceramics Using a Composite Approach. *ACS Appl. Mater. Interfaces* **15**, 36576–36586 (2023).
42. Zhang, Y. et al. Grain Boundary Diffusion Hardening in Potassium Sodium Niobate-Based Ceramics with Full Gradient Composition and High Piezoelectricity. *Adv. Funct. Mater.* **33**, 2306039 (2023).
43. Guan, Y. et al. Superior Electromechanical Compatibility in Lead-Free Piezoceramics with Mobile Transition-Metal Defects. *ACS Appl. Mater. Interfaces* **15**, 51421–51428 (2023).
44. Liu, C. et al. Electrical Properties of CuO-doped $(\text{K}_{0.5}\text{Na}_{0.5})(\text{Nb}_{0.92}\text{Sb}_{0.03}\text{Ta}_{0.05})\text{O}_3$ Piezoelectric Ceramics with High Q_m . *Ferroelectrics* **458**, 31–36 (2014).
45. Ren, X. Large electric-field-induced strain in ferroelectric crystals by point-defect-mediated reversible domain switching. *Nat. Mater.* **3**, 91–94 (2004).
46. Dong, J. et al. Continuous electroproduction of formate via CO_2 reduction on local symmetry-broken single-atom catalysts. *Nat. Commun.* **14**, 6849 (2023).
47. Hai, X. et al. Geminal-atom catalysis for cross-coupling. *Nature* **622**, 754–760 (2023).
48. Lin, J. et al. Tailoring micro-structure of eco-friendly temperature-insensitive transparent ceramics achieving superior piezoelectricity. *Acta Mater.* **235**, 118061 (2022).
49. Lin, J. et al. Ultrahigh energy harvesting properties in temperature-insensitive eco-friendly high-performance KNN-based textured ceramics. *J. Mater. Chem. A* **10**, 7978–7988 (2022).
50. Hu, Q., Du, H., Feng, W., Chen, C. & Huang, Y. Studying the roles of Cu and Sb in $\text{K}_{0.46}\text{Na}_{0.52}\text{NbO}_3$ lead-free piezoelectric ceramics. *J. Alloy. Compd.* **640**, 327–334 (2015).

51. Yin, M. et al. Microscopic origin of the enhanced piezoelectric thermal stability in acceptor doped lead-free Ba(Ti_{0.8}Zr_{0.2})O₃-50(Ba_{0.7}Ca_{0.3})TiO₃ ceramic. *Ceram. Int.* **48**, 5274–5279 (2022).
52. Zhang, L. & Ren, X. Aging Behavior in Single-Domain Mn-Doped BaTiO₃ Crystals: Implication for a Unified Microscopic Explanation of Ferroelectric Aging. *Phys. Rev. B* **73**, 094121 (2006).
53. Yang, L. et al. Simultaneously achieving giant piezoelectricity and record coercive field enhancement in relaxor-based ferroelectric crystals. *Nat. Commun.* **13**, 2444 (2022).
54. Shujun, Z., Alberta, E. F., Eitel, R. E., Randall, C. A. & Shrout, T. R. Elastic, piezoelectric, and dielectric characterization of modified BiScO₃-PbTiO₃ ceramics. *IEEE Trans. Ultrason. Ferroelectr. Freq. Control* **52**, 2131–2139 (2005).
55. Du, Y. et al. XAFCA: a new XAFS beamline for catalysis research. *J. Synchrotr. Radiat.* **22**, 839–843 (2015).
56. Ravel, B. & Newville, M. ATHENA, ARTEMIS, HEPHAESTUS: data analysis for X-ray absorption spectroscopy using IFEFFIT. *J. Synchrotr. Radiat.* **12**, 537–541 (2005).
57. Bunău, O. & Joly, Y. Self-consistent aspects of x-ray absorption calculations. *J. Phys.: Condens. Matter* **21**, 345501 (2009).
58. Kresse, G. & Hafner, J. Ab initio molecular-dynamics simulation of the liquid-metal-amorphous-semiconductor transition in germanium. *Phys. Rev. B* **49**, 14251–14269 (1994).
59. Kresse, G. & Furthmüller, J. Efficient iterative schemes for ab initio total-energy calculations using a plane-wave basis set. *Phys. Rev. B* **54**, 11169–11186 (1996).
60. Perdew, J. P. et al. Restoring the Density-Gradient Expansion for Exchange in Solids and Surfaces. *Phys. Rev. Lett.* **100**, 136406 (2008).
61. Blöchl, P. E. Projector augmented-wave method. *Phys. Rev. B* **50**, 17953–17979 (1994).

Acknowledgements

This work was financially supported by the National Natural Science Foundation of China (Grant Nos. U23A20567 and 12204327), the Natural Science Foundation of Sichuan Province (Grant Nos. 2023NSFSC0967 and 2024NSFJQ0025), the Opening Project of Key Laboratory of Inorganic Functional Materials and Devices, Chinese Academy of Sciences (Grant No. KLIFMD202306), the Open Project Fund from Guangdong Provincial Key Laboratory of Materials and Technologies for Energy Conversion, Guangdong Technion-Israel Institute of Technology (Grant No. MATEC2024KF007), the Guangdong Province Science and Technology Major Project (Grant No. 2021B0301030005), and the State Key Laboratory of Powder Metallurgy, Central South University, Changsha, China. The authors thank Ms. Hui Wang (the Analytical & Testing Center of Sichuan University) for conducting the FE-SEM measurements.

Author contributions

The work was conceived and designed by X.Q., X.L. and J.W., with the sample fabrication carried out by X.Q. and X.L. They also performed

dielectric, piezoelectric, and ferroelectric properties measurements and analyzed the corresponding data. XRD patterns and Raman spectra were performed by Y.M. and X.-X.Z. PFM images were captured and processed by X.L. TEM images of ferroelectric domains were measured by S.W. and J.Z. STEM-HAADF images were measured by C.L. and X.-X.Z. and were processed by Z.W. X.A.F.S. measurements were performed by C.W. for data collection and processing, and DFT calculations were conducted by Z.T. The paper was drafted by X.Q., with modifications made by R.L., D.-Q.T., X.L., Z.W., and J.W. All authors contributed to data analysis and discussion.

Competing interests

The authors declare no competing interests.

Additional information

Supplementary information The online version contains supplementary material available at <https://doi.org/10.1038/s41467-025-58269-5>.

Correspondence and requests for materials should be addressed to Daniel Q. Tan, Zhipeng Wang, Xiang Lv or Jiagang Wu.

Peer review information *Nature Communications* thanks Lucjan Kozielski, Alexander Martin, and the other, anonymous, reviewer(s) for their contribution to the peer review of this work. A peer review file is available.

Reprints and permissions information is available at <http://www.nature.com/reprints>

Publisher's note Springer Nature remains neutral with regard to jurisdictional claims in published maps and institutional affiliations.

Open Access This article is licensed under a Creative Commons Attribution-NonCommercial-NoDerivatives 4.0 International License, which permits any non-commercial use, sharing, distribution and reproduction in any medium or format, as long as you give appropriate credit to the original author(s) and the source, provide a link to the Creative Commons licence, and indicate if you modified the licensed material. You do not have permission under this licence to share adapted material derived from this article or parts of it. The images or other third party material in this article are included in the article's Creative Commons licence, unless indicated otherwise in a credit line to the material. If material is not included in the article's Creative Commons licence and your intended use is not permitted by statutory regulation or exceeds the permitted use, you will need to obtain permission directly from the copyright holder. To view a copy of this licence, visit <http://creativecommons.org/licenses/by-nc-nd/4.0/>.

© The Author(s) 2025